Journal of Marine Science and Technology

Volume 17 | Issue 2 Article 8

INDUCTIVELY/CAPACITIVELY COUPLED CONDUCTOR-BACKED COPLANAR WAVEGUIDE BANDPASS FILTERS USING SLOW-WAVE STEPPED-IMPEDANCE RESONATORS

Jiunn-Jye Chang
Department of Electrical Engineering, National Taiwan Ocean University, Keelung, Taiwan, R.O.C.,
jjchang@mail.ntou.edu.tw

Chih-Hong Sie
Department of Electrical Engineering, National Taiwan Ocean University, Keelung, Taiwan, R.O.C.

INDUCTIVELY/CAPACITIVELY COUPLED CONDUCTOR-BACKED COPLANAR WAVEGUIDE BANDPASS FILTERS USING SLOW-WAVE STEPPED-IMPEDANCE RESONATORS

Jiunn-Jye Chang* and Chih-Hong Sie*

Key words: conductor-backed coplanar waveguide, slow-wave structure, stepped-impedance resonator, defected ground structure, bandpass filter.

ABSTRACT

In this paper, using the conductor-backed coplanar waveguides (CBCPWs) and the slow-wave stepped-impedance resonators, a second-order and a fourth-order inductively/capacitively coupled bandpass filters are designed, implemented, and measured. For second-order bandpass filter, two H-shaped defected ground structure (DGS) patterns are etched on the backside metallic ground planes of the input and output feedlines, it is found that two attenuation poles exist on both sides of the passband. When compared to the fourth-order bandpass filter without H-shaped DGS, the second-order bandpass filter with H-shaped DGS has compact size and comparable rolloff at the edges of the passband. In addition, the measured results of the filters agree well with the simulated ones.

I. INTRODUCTION

The uniform impedance resonators (UIRs) have been widely applicated in the design of microwave circuits. But a UIR seriously suffers from spurious harmonics in addition to its relative large size. A stepped-impedance resonator (SIR) exhibits advantages in size reduction and good spurious characteristics when compared to a UIR [10, 8]

Coplanar waveguides (CPWs) have several advantages over conventional microstrip lines, including no need of via-holes, easy connection of both series and shunt components, low dispersion and radiation loss, and so on [5]. Furthermore, due to an additional backside metallic ground plane, the conductorbacked coplanar waveguides (CBCPWs) could improve both the power-handling capability and the mechanical strength of the integrated circuit [2].

Paper submitted 11/30/07; accepted 07/11/08. Author for correspondence: Jiunn-Jye Chang (e-mail: jjchang@mail.ntou.edu.tw).

**Department of Electrical Engineering, National Taiwan Ocean University, Keelung, Taiwan, R.O.C.*

In the equivalent circuit of the defected ground structure (DGS), there are a series inductor and a shunt capacitor, so the DGS exhibits a bandstop response. Although the open or short stub also exhibits a bandstop response, but it can't reduce the circuit size. Recently, the DGSs have been extensively studied to further reduce the circuit size and improve the stopband characteristics of the filters [6, 7, 1]. To date, the slow-wave CBCPW SIR and the CBCPW with DGS have not been studied to design microwave circuits. In this paper, the slow-wave CBCPW SIR and the CBCPW with H-shaped DGS are studied firstly and then used to design two inductively/capacitively coupled bandpass filters, one is second-order with H-shaped DGS and the other is fourth-order without H-shaped DGS.

II. SLOW-WAVE CBCPW SIR

The basic structure of the slow-wave CBCPW SIR is shown in Fig. 1, where $Z_1 > Z_3 > Z_2$ is assumed. Due to the smallest impedance among the three CBCPW sections, the midsection can be embedded into the upside metallic ground plane and introduce slow-wave effect, which can reduce the size of the circuit.

The input admittance (Y_i) looking into the right port of the SIR can be expressed as [11]

$$Y_i = \frac{Z_2 Z_3 - Z_1 Z_3(\tan\theta_1)(\tan\theta_2) - Z_1 Z_2(\tan\theta_1)(\tan\theta_3) - Z_2^2(\tan\theta_2)(\tan\theta_3)}{\Delta} \tag{1}$$

$$\Delta = jZ_1 Z_2 Z_3 \tan\theta_1 + jZ_2^2 Z_3 \tan\theta_2 + jZ_2 Z_3^2 \tan\theta_3 - jZ_1 Z_3^2(\tan\theta_1)(\tan\theta_2)(\tan\theta_3) \tag{2}$$

where Z_1, Z_2, Z_3 are the characteristic impedances of the three CBCPW sections, and θ_1, θ_2, θ_3 are the corresponding electrical lengths. At resonance, $Y_i = 0$ and the resonance condition is

$$\frac{Z_1}{Z_2}(\tan\theta_1)(\tan\theta_2) + \frac{Z_1}{Z_3}(\tan\theta_1)(\tan\theta_3) + \frac{Z_2}{Z_3}(\tan\theta_2)(\tan\theta_3) = 1. \tag{3}$$

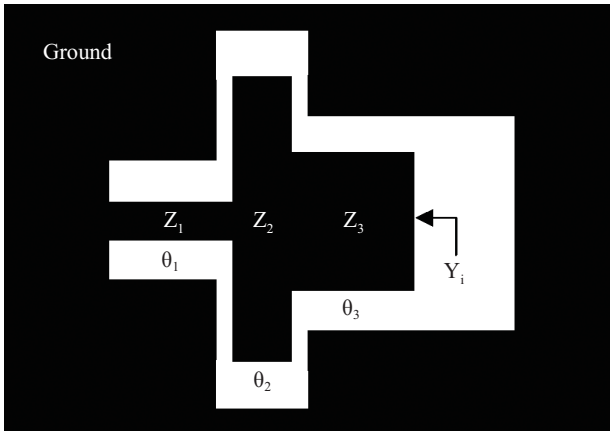

Fig. 1. Structure of the slow-wave CBCPW SIR.

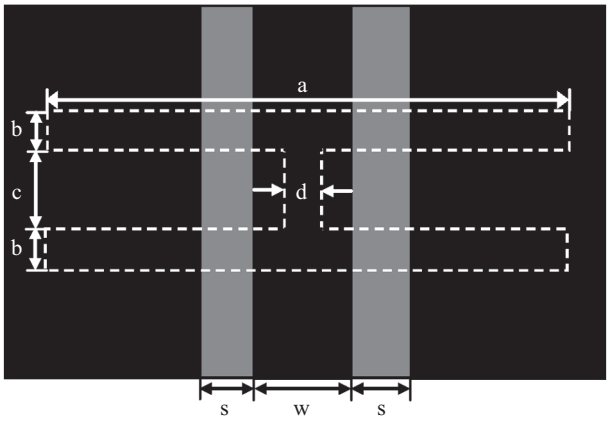

Fig. 2. Structure of the CBCPW with H-shaped DGS.

For simplicity consideration, $\theta_1 = \theta_3$ is assumed. The total electrical length (θ_t) of the slow-wave CBCPW SIR is expressed as

$$\theta_t = \theta_1 + \theta_2 + \theta_3 = 2\theta_1 + \tan^{-1}\left[\frac{Z_2 Z_3 - Z_1 Z_2 \tan^2\theta_1}{\left(Z_1 Z_3 + Z_2^{\,2}\right)\tan\theta_1}\right]. \quad (4)$$

The total electrical length (θ_t) of the slow-wave CBCPW SIR is a function of Z_1, Z_2, Z_3, and θ_1. When Z_1, Z_2, and Z_3 are fixed, θ_t is only a function of θ_1.

III. CBCPW WITH H-SHAPED DGS

The structure of the CBCPW with H-shaped DGS pattern etched on the backside metallic ground plane is shown in Fig. 2.

Based on a DICLAD-880 substrate with ε_r = 2.17 and h = 0.635 mm, the slow-wave factor of the CBCPW with H-shaped DGS and the frequency responses of $|S_{11}|$ and $|S_{21}|$ simulated by the full-wave EM simulator Sonnet are plotted in

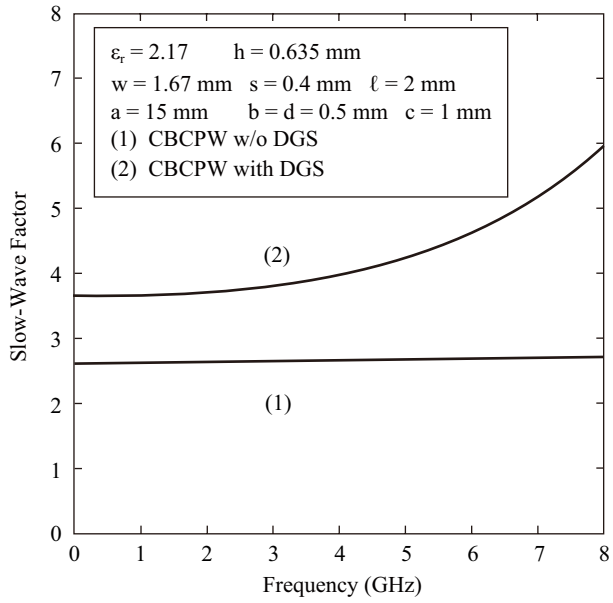

Fig. 3. The slow-wave factor of the CBCPW with H-shaped DGS.

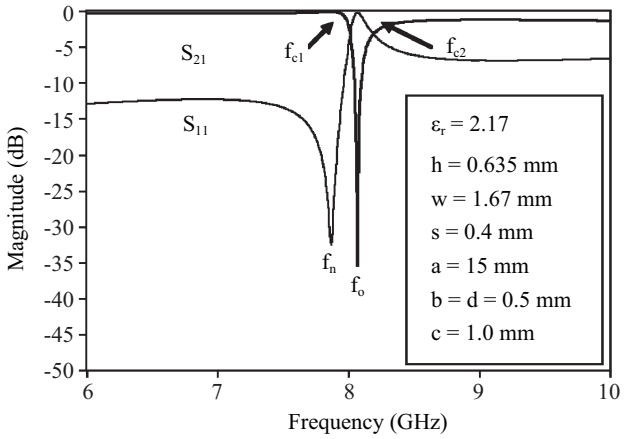

Fig. 4. Frequency response of the CBCPW with the H-shaped DGS.

Figs. 3 and 4, respectively. From Fig. 3, it is found that the slow-wave factor is apparently increased due to the insertion of H-shaped DGS. In other words, the H-shaped DGS has the slow-wave effect and can reduce the circuit size. From Fig. 4, in the $|S_{21}|$ response, f_o is the frequency of attenuation pole, f_{c1} and f_{c2} are the lower and upper 3-dB cutoff frequencies, respectively. Besides, f_n is the notch frequency in the $|S_{11}|$ response. In other words, the CBCPW with H-shaped DGS exhibits a bandstop response and has sharp cutoff characteristics.

From the simulation results, it is found that the influences of the length (a) of the H-shaped DGS are more pronounced, but those of the rest structure parameters (b, c, and d) are less pronounced. In other words, the length of the H-shaped DGS is the dominant structure parameter to determine the frequency of attenuation pole.

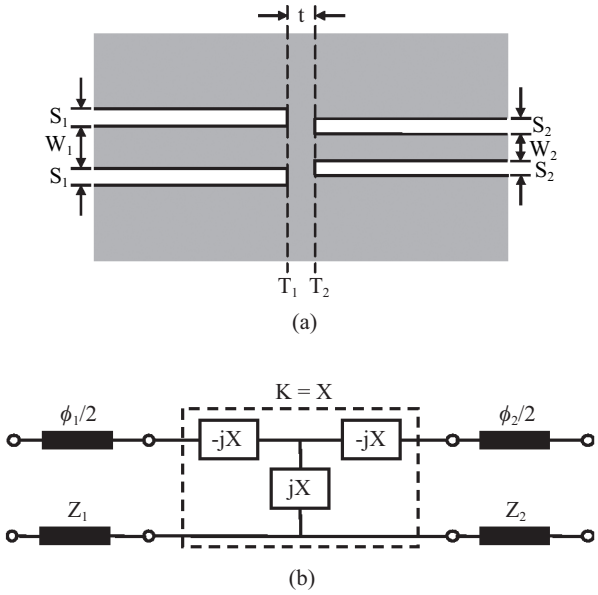

Fig. 5. CPW inductive coupling structure. (a) Coupling structure. (b) Equivalent *K*-inverter.

IV. CPW COUPLING STRUCTURES

The inductive and capacitive coupling structures are usually utilized in the design of directly coupled filters [3, 4, 12]. Figure 5(a) shows the CPW inductive coupling structure, where W_1 and W_2 are the strip widths, and S_1 and S_2 are the slot widths of the two different CPWs. In addition, t is the coupling length, and T_1 and T_2 are two reference planes. Based on the analysis of Z-parameters, the equivalent K-inverter is shown in Fig. 5(b), where the normalized K-inverter impedance $\left(\frac{K}{\sqrt{Z_1 Z_2}}\right)$ and the electrical lengths (ϕ_1 and ϕ_2) can be written as

$$\frac{K}{\sqrt{Z_1 Z_2}} = \frac{\sin\left(\frac{\phi_1}{2}\right) + \overline{X}_{11}\cos\left(\frac{\phi_1}{2}\right)}{\overline{X}_{12}\sin\left(\frac{\phi_2}{2}\right)} \tag{5}$$

$$\phi_1 = -\tan^{-1}\left[\frac{2(\overline{X}_{11} + \overline{X}_{22}\left|\overline{X}\right|)}{(1+\overline{X}_{22}^2 - \overline{X}_{11}^2 - \left|\overline{X}\right|^2)}\right] \tag{6}$$

$$\phi_2 = -\tan^{-1}\left[\frac{2(\overline{X}_{22} + \overline{X}_{11}\left|\overline{X}\right|)}{(1+\overline{X}_{11}^2 - \overline{X}_{22}^2 - \left|\overline{X}\right|^2)}\right] \tag{7}$$

where $\overline{X}_{11} = X_{11}/Z_1$, $\overline{X}_{22} = X_{22}/Z_2$, $\overline{X}_{12} = X_{12}/\sqrt{Z_1 Z_2}$, and $\left|\overline{X}\right| = \overline{X}_{11}\overline{X}_{22} - \overline{X}_{12}^2$. Besides, X_{11}, X_{22}, X_{12} are the imaginary parts of Z_{11}, Z_{22}, Z_{12}, respectively, and Z_1 and Z_2 are the characteristic impedances of the two CPWs. If these two CPWs are the same, that is $W_1 = W_2$ and $S_1 = S_2$, the normalized K-inverter impedance and electrical lengths are given by (5)-(7) with the substitution of $Z_1 = Z_2$ and $X_{11} = X_{22}$.

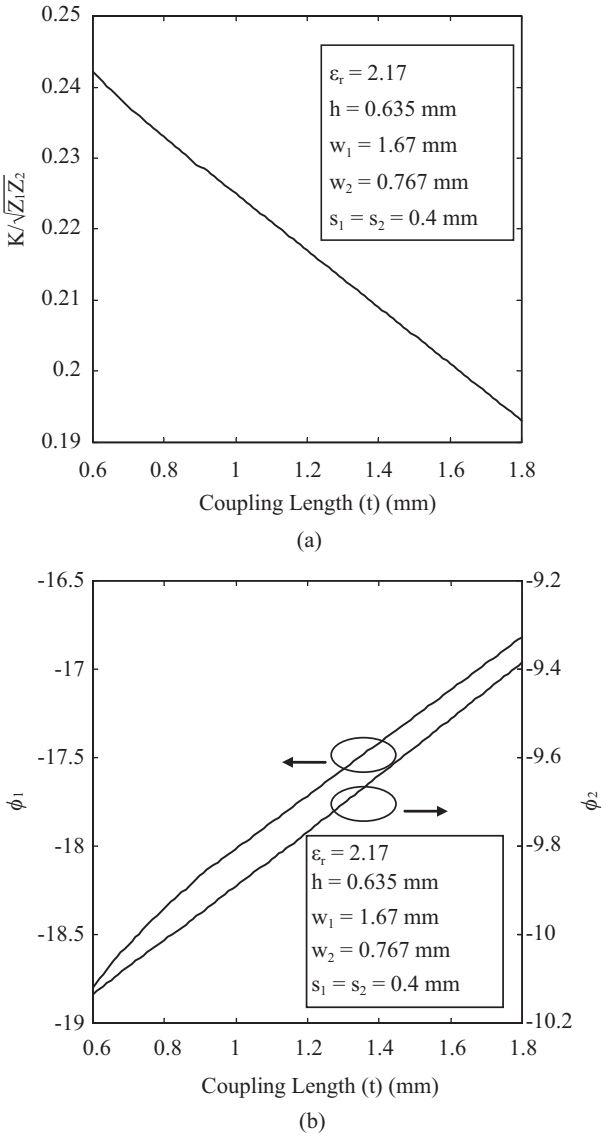

Fig. 6. *K*-inverter parameters as a function of coupling length. (a) Normalized *K*-inverter impedance. (b) Electrical length.

The simulated results of the normalized K-inverter impedance $\left(\frac{K}{\sqrt{Z_1 Z_2}}\right)$ and the electrical lengths (ϕ_1 and ϕ_2) as a function of the coupling length (t) are plotted in Figs. 6(a) and 6(b), respectively. From the simulation results, it can be seen that the normalized K-inverter impedance decreases when the coupling length increases. But, the electrical lengths increase with the coupling length.

On the other hand, Fig. 7(a) shows the CPW capacitive coupling structure, where W and S are the strip and slot widths,

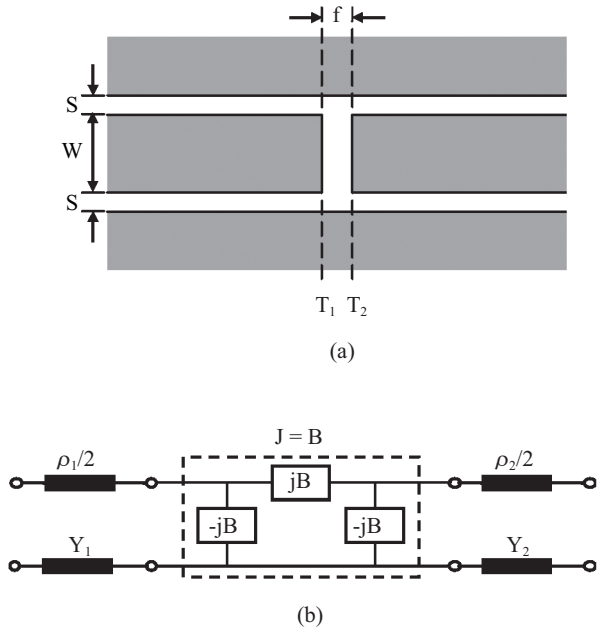

Fig. 7. CPW capacitive coupling structure. (a) Coupling structure. (b) Equivalent *K*-inverter.

respectively, of the two CPWs. In addition, f is the coupling length, and T_1 and T_2 are two reference planes. On the basis of the analysis of *Y*-parameters, the equivalent *J*-inverter is shown in Fig. 7(b), where the normalized *J*-inverter admittance $\left(\frac{J}{\sqrt{Y_1Y_2}}\right)$ and the electrical lengths (ρ_1 and ρ_2) can be expressed as

$$\frac{J}{\sqrt{Y_1Y_2}} = \frac{\sin\left(\frac{\rho_1}{2}\right) + \overline{B}_{11}\cos\left(\frac{\rho_1}{2}\right)}{\overline{B}_{12}\sin\left(\frac{\rho_2}{2}\right)} \tag{8}$$

$$\rho_1 = -\tan^{-1}\left[\frac{2(\overline{B}_{11} + \overline{B}_{22}|\overline{B}|)}{(1+\overline{B}_{22}^2 - \overline{B}_{11}^2 - |\overline{B}|^2)}\right] \tag{9}$$

$$\rho_2 = -\tan^{-1}\left[\frac{2(\overline{B}_{22} + \overline{B}_{11}|\overline{B}|)}{(1+\overline{B}_{11}^2 - \overline{B}_{22}^2 - |\overline{B}|^2)}\right] \tag{10}$$

where $\overline{B}_{11} = B_{11}/Y_1$, $\overline{B}_{22} = B_{22}/Y_2$, $\overline{B}_{12} = B_{12}/\sqrt{Y_1Y_2}$, and $|\overline{B}| = \overline{B}_{11}\overline{B}_{22} - \overline{B}_{12}^2$. In addition, B_{11}, B_{22}, B_{12} are the imaginary parts of Y_{11}, Y_{22}, Y_{12}, respectively, and Y_1 and Y_2 are the characteristic admittances of the two CPWs. The two CPWs, as shown in Fig. 6(b), have the same strip and slot widths, respectively, so $Y_1 = Y_2$ and $B_{11} = B_{22}$.

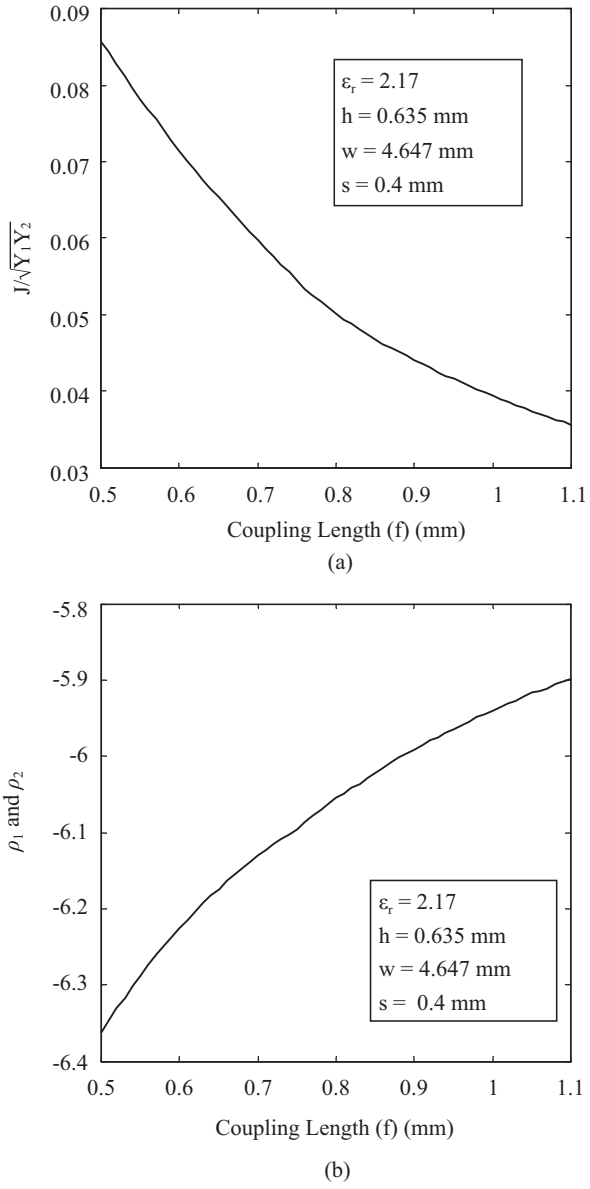

Fig. 8. *J*-inverter parameters as a function of coupling length. (a) Normalized *J*-inverter admittance. (b) Electrical length.

The simulated results of the normalized *J*-inverter admittance $\left(\frac{J}{\sqrt{Y_1Y_2}}\right)$ and the electrical lengths (ρ_1 and ρ_2) versus the coupling length (f) are plotted in Figs. 8(a) and 8(b), respectively. From Fig. 8, it can be seen that when the coupling length increases, the normalized *J*-inverter admittance decreases but the electrical lengths increase.

V. NTH-ORDER BANDPASS FILTER WITH $\lambda/4$ RESONATORS

Based on the filter theory, the coupling coefficients of the inductive and capacitive coupling structures in the *N*th-order bandpass filter with $\lambda/4$ resonators can be expressed as [9].

$$K_{01} = \sqrt{\frac{\pi\Delta}{4g_0 g_1}} \tag{11}$$

$$J_{i,i+1} \text{ or } K_{i,i+1} = \frac{\pi\Delta}{4\sqrt{g_i g_{i+1}}}, \; i = 1, 2, ..., (N-1) \tag{12}$$

$$J_{N,N+1}\big|_{N \text{ is odd}} \text{ or } K_{N,N+1}\big|_{N \text{ is even}} = \sqrt{\frac{\pi\Delta}{4g_N g_{N+1}}} \tag{13}$$

where Δ is the 3-dB fractional bandwidth, and g_i (i = 0, 1, 2, …, N + 1) are the prototype element values of the lowpass filter. K_{01} is the inductive coupling coefficient between the input feedline and the first resonator, $J_{i,I+1}$ or $K_{i,I+1}$ is the capacitive or inductive coupling coefficient between the adjacent resonators. In addition, $J_{N,N+1}$ or $K_{N,N+1}$ is the capacitive or inductive coupling coefficient between the last resonator and the output feedline. If the ith coupling structure is inductive, the electrical length (θ_{ci}) of the ith resonator is given by

$$\theta_{ci} = \theta_t + \frac{1}{2}(\phi_i + \rho_{i+1}), \; i = 1, 2, ..., N \tag{14}$$

where θ_t, ϕ_1 and ρ_{i+1} are given by (4), (7), and (9), respectively. On the other hand, if the ith coupling structure is capacitive, the electrical length (θ_{ci}) of the ith resonator is given by

$$\theta_{ci} = \theta_t + \frac{1}{2}(\phi_{i+1} + \rho_i), \; i = 1, 2, ..., N \tag{15}$$

where θ_t, ϕ_{i+1} and ρ_i are given by (4), (6), and (10), respectively.

VI. INDUCTIVELY/CAPACITIVELY COUPLED CBCPW BANDPASS FILTER

In this paper, the slow-wave CBCPW SIRs are used to design two inductively/capacitively coupled bandpass filters, one is second-order with H-shaped DGS and the other is fourth-order without H-shaped DGS. All the designs are fabricated on DICLAD-880 substrates with dielectric constant (ε_r) of 2.17, thickness (h) of 0.635 mm, and loss tangent of 0.0008 @10 GHz.

1. Design Procedure

Step 1. According to the design parameters of the two bandpss filters, determine the prototype element values (g_i) of the lowpass filters. In this paper, both two filters have the center frequency of 6 GHz, 3-dB fractional bandwidth of 6%, and passband ripple of 0.1 dB in the Chebyshev response. In addition, for the second-order bandpass filter with H-shape DGS, there are two attenuation poles on both sides of the passband, one at 5.5 GHz and the other at 6.5 GHz. As a result, $g_0 = 0$, $g_1 = 0.8431$, $g_2 = 0.6220$, $g_3 = 1.3554$ for the second-order case, and $g_o = 1$, $g_1 = 1.1088$, $g_2 = 1.3062$, $g_3 = 1.7704$, $g_4 = 0.8181$, $g_5 = 1.3554$ for the fourth-order case.

Step 2. Determine the inductive and capacitive coupling coefficients (K and J), the coupling lengths (t and f), and the electrical lengths (ϕ and ρ) of the equivalent K- and J-inverters, respectively. As a result, for the second-order case, $K_{01} = K_{23} = 0.2364$, $J_{12} = 0.0651$; $t_{01} = t_{23} = 0.72$ mm, $f_{12} = 0.66$ mm; $\phi_{01} = \phi_{23} = -10.05°$, $\rho_{12} = -6.17°$. For the fourth-order case, $K_{01} = K_{45} = 0.2062$, $K_{23} = 0.0301$, $J_{12} = J_{34} = 0.0392$; $t_{01} = t_{45} = 1.47$mm, $t_{23} = 2.75$ mm, $f_{12} = f_{34} = 1.01$ mm, and $\phi_{01} = \phi_{45} = -9.53°$, $\phi_{23} = -7.59°$, $\rho_{12} = \rho_{34} = -5.94°$.

Step 3. Select the values of Z_1, Z_2, and Z_3 in the slow-wave CBCPW SIR, and determine the corresponding electrical lengths θ_1, θ_2, and θ_3. In this paper, $Z_1 = 75\ \Omega$, $Z_2 = 20\ \Omega$, $Z_3 = 25\ \Omega$, and $\theta_1 = \theta_3 = 26.93°$, $\theta_2 = 5.35°$. Furthermore, calculate the final electrical length (θ_{ci}) of each slow-wave CBCPW SIR, including the equivalent K- or J-inverter parameters (ϕ or ρ). As a result, for the second-order case, $\theta_{c1} = \theta_{c2} = 51.10°$. For the fourth-order case, there are four slow-wave CBCPW SIRs, $\theta_{c1} = \theta_{c4} = 51.48°$ and $\theta_{c2} = \theta_{c3} = 55.45°$.

Step 4. Determine the strip width (W) and the slot width (S) of each CBCPW in the slow-wave SIR. The calculated results for 75 Ω, 20 Ω, and 25 Ω CBCPWs are $W_1 = 0.77$ mm, $W_2 = 6.44$ mm, $W_3 = 4.65$ mm, and $S_1 = 0.4$ mm, $S_2 = 0.8$ mm, $S_3 = 0.4$ mm.

Step 5. Determine the structure parameters (a, b, c, and d) of the two H-shaped DGSs in the second-order bandpass filter. For introducing two attenuation poles at 5.5 GHz and 6.5 GHz, two H-shaped DGS patterns are etched on the backside metallic ground planes of the input and output feedlines. For attenuation pole at 5.5 GHz, the H-shaped DGS parameters are $a_1 = 19.79$ mm, $b_1 = 0.5$ mm, $c_1 = 0.6$ mm, and $d_1 = 0.5$ mm. On the other hand, the H-shaped DGS parameters are $a_2 = 16.52$ mm, $b_2 = 0.5$ mm, $c_2 = 0.6$ mm, and $d_2 = 0.5$ mm for attenuation pole at 6.5 GHz.

Step 6. Using the full-wave EM simulator Sonnet to simulate each bandpass filter.

2. Simulated Results

The layout of the second-order banspass filter with H-shaped DGS is shown in Fig. 9(a). The dimensions of the filter are $w_{50} = 1.67$ mm, $w_1 = 0.77$ mm, $w_2 = 6.44$ mm, $w_3 = 4.65$ mm, $s_{50} = 0.4$ mm, $s_1 = s_3 = 0.4$ mm, $s_2 = 0.8$ mm, $\ell_{50} = 5.5$ mm, $\ell_1 = 1.51$ mm, $\ell_2 = \ell_5 = 0.52$ mm, $\ell_3 = \ell_4 = 1.52$ mm, $\ell_6 = 1.52$ mm, $g_1 = g_2 = 0.4$ mm, $t_1 = 0.74$ mm, $t_2 = 0.71$ mm, $f_1 = 0.66$ mm, $a_1 = 19.79$ mm, $a_2 = 16.52$ mm, $b_1 = b_2 = 0.5$ mm, $c_1 = c_2 = 0.6$ mm, $d_1 = d_2 = 0.5$ mm. The overall size of the filter is 20.2 mm × 23 mm. Figure 9(b) shows the simulated frequency response of the filter. It is found that the center frequency is

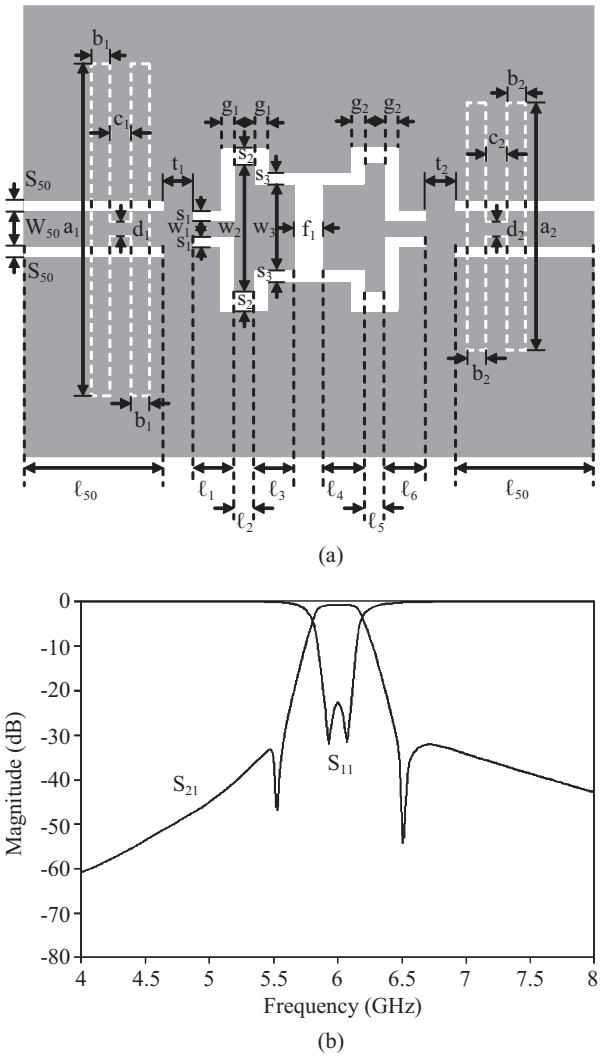

Fig. 9. Simulated results of the second-order bandpass filter with H-shaped DGS. (a) Filter layout. (b) Frequency response.

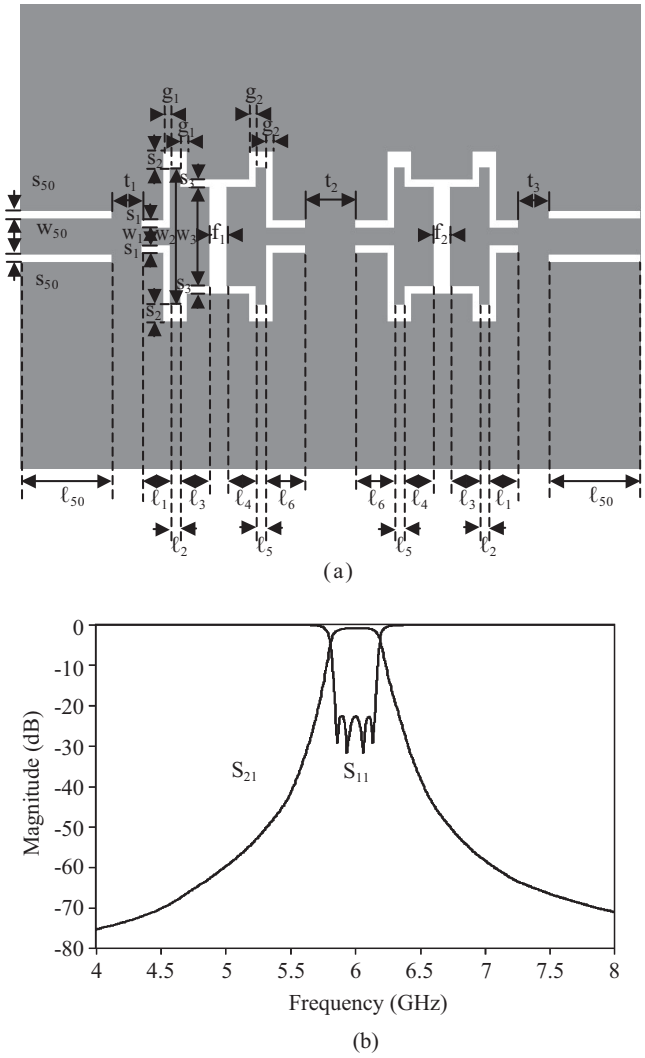

Fig. 10. Simulated results of the fourth-order bandpass filter without H-shaped DGS. (a) Filter layout. (b) Frequency response.

5.99 GHz and the 3-dB bandwidth is 365 MHz. The insertion loss is less than 0.91 dB and the return loss is better than 23.2 dB in the passband. Due to two H-shaped DGS patterns etched on the backside metallic ground planes of the input and output feedlines, which won't give rise to extra circuit dimension, there are two attenuation poles exist at 5.5 GHz and 6.5 GHz in the simulated $|S_{21}|$ response. In addition, the attenuations at the two poles are 47.1 dB and 53.9 dB, respectively.

On the other hand, the layout of the fourth-order filter without H-shaped DGS is shown in Fig. 10(a). The dimensions of the filter are w_{50} = 1.67 mm, w_1 = 0.77 mm, w_2 = 6.44 mm, w_3 = 4.65 mm, s_{50} = 0.4 mm, $s_1 = s_3$ = 0.4 mm, s_2 = 0.8 mm, ℓ_{50} = 5.0 mm, ℓ_1 = 1.58 mm, $\ell_2 = \ell_5$ = 0.52 mm, $\ell_3 = \ell_4$ = 1.57 mm, ℓ_6 = 2.15 mm, $g_1 = g_2$ = 0.4 mm, $t_1 = t_3$ = 1.61 mm, t_2 = 2.68 mm, $f_1 = f_2$ = 0.96 mm. The simulated frequency response of the filter is shown in Fig. 10(b). The overall size of the filter is 36.6 mm × 22 mm. It is noted that the filter has the center frequency of 5.98 GHz and 3-dB bandwidth of 368 MHz. In the passband, the insertion loss is less than 0.92 dB and the return loss is better than 22.8 dB. The attenuations at 5.5 GHz and 6.5 GHz are 41.5 dB and 37.9 dB, respectively.

The comparison between the simulated frequency responses of the two filters is shown in Fig. 11. There are two attenuation poles, one at 5.5 GHz and the other at 6.5 GHz, on both sides of the passband in the second-order bandpass filter with H-shaped DGS. The attenuations at 5.5 GHz and 6.5 GHz in the second-order bandpass filter with H-shaped DGS are greater than those in the fourth-order case. Furthermore, it is observed that the rolloff at the edges of the passband in the second-order bandpass filter with H-shaped DGS is comparable to that in the fourth-order case. On the other hand, the circuit size of the second-order bandpass filter with H-shaped DGS is 37.3% smaller than that of the fourth-order case. In addition, the filters designed using CBCPW, slow-wave SIR, and DGS do much more performances when compared with other types of CPW filters.

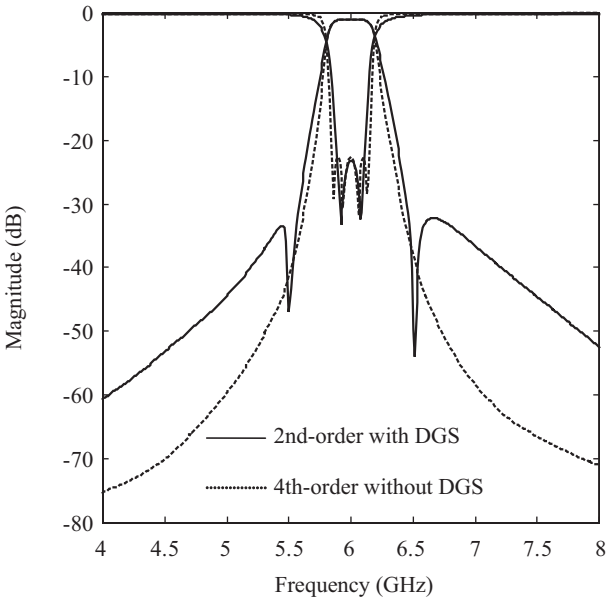

Fig. 11. Comparison between the simulated frequency responses of the two filters.

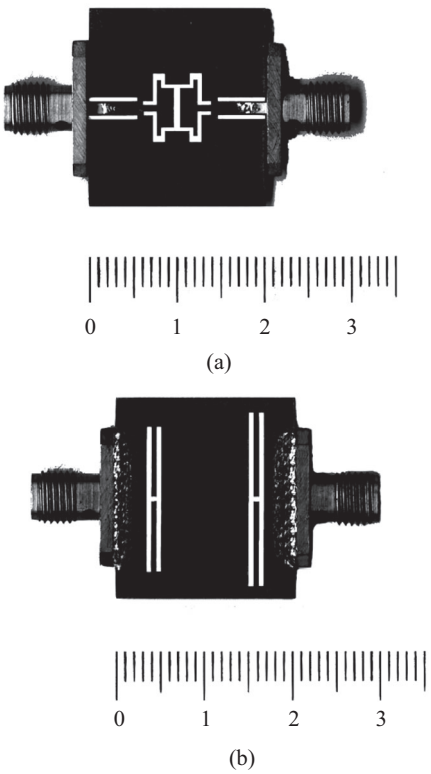

Fig. 12. Implemented second-order bandpass filter with H-shaped DGS. (a) Top view. (b) Bottom View.

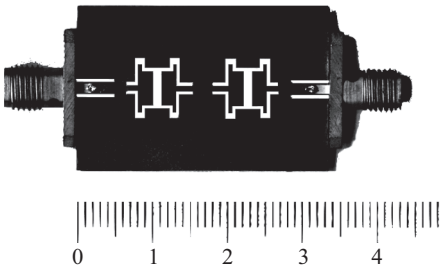

Fig. 13. Implemented fourth-order bandpass filter without H-shaped DGS.

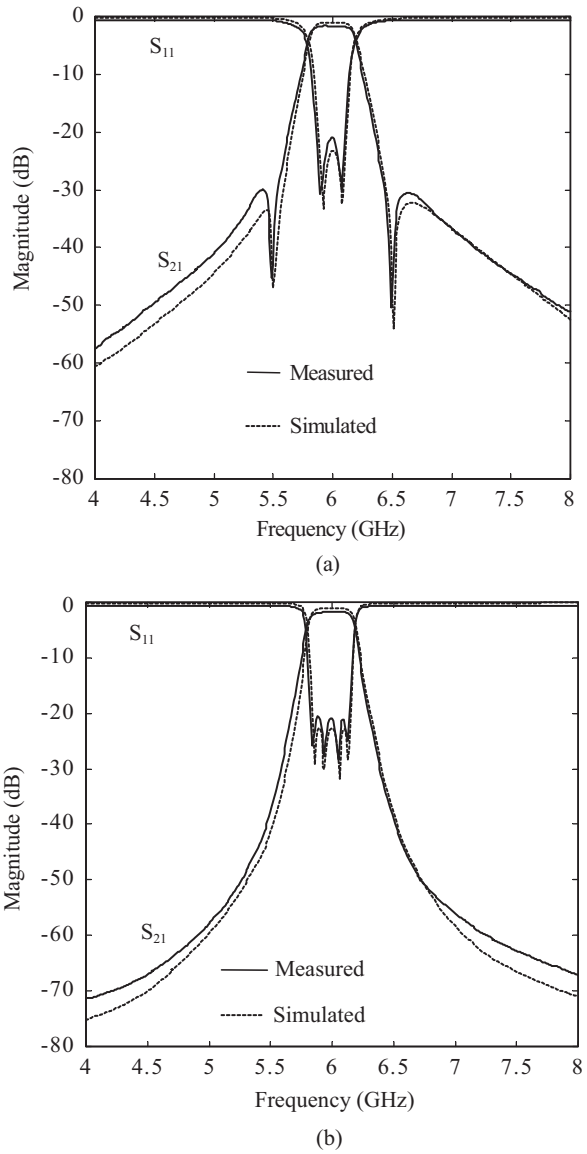

Fig. 14. Measured and simulated results of the two bandpass filters. (a) Second-order with DGS. (b) Fourth-order without DGS.

3. Measured Results

The two implemented bandpass filters are shown in Figs. 12 and 13, respectively. The measured results of the two bandpass filters are shown in Fig. 14, where the simulated results are also drawn for comparison. For the second-order bandpass filter with H-shaped DGS, the center frequency is 5.98 GHz and the 3-dB bandwidth is 368 MHz. In the passband, the

insertion loss is less than 1.46 dB and the return loss is better than 20.9 dB. Furthermore, the attenuations at the two poles, which are measured at 5.49 GHz and 6.49 GHz, are 45.2 dB and 50.4 dB, respectively. In addition, the measured results agree well with the simulated ones.

On the other hand, the fourth-order bandpass filter without H-shaped DGS has the center frequency of 5.97 GHz and 3-dB bandwidth of 371 MHz. The insertion loss is less than 1.56 dB and the return loss is better than 20.1 dB in the passband. Furthermore, the measured attenuations at 5.5 GHz and 6.5 GHz are 37.2 dB and 38.9 dB, respectively. In addition, the discrepancy between the measured and simulated results is small.

VII. CONCLUSION

Using the slow-wave CBCPW SIRs, a second-order with H-shaped DGS and a fourth-order without H-shaped DGS inductively/capacitively coupled bandpass filters have been designed, implemented, and measured. Agreement between the simulated and measured results has been shown to be well. Since two H-shaped DGS patterns were etched on the backside metallic ground planes of the input and output feedlines in the second-order bandpass filter, it has been found that two attenuation poles exist on both sides of the passband.

Furthermore, the second-order bandpass filter with H-shaped DGS has comparable rolloff at the edges of the passband in addition to its relative compact size when compared to the fourth-order case. Additionally, it is expected that the present method can be applicated to reduce the circuit size and improve the performances of other microwave circuits.

REFERENCES

1. Akgun, O. and Gorur, A., "Slow-wave CPW resonator with defected ground structure (DGS) for filter applications," *Microwave and Optical Technology Letters*, Vol. 48, No. 2, pp. 229-233 (2006).
2. Cheng, K. K. M. and Everard, J. K. A., "A new technique for the quasi-TEM analysis of conductor-backed coplanar waveguide structures," *IEEE Transactions on Microwave Theory and Techniques*, Vol. 41, No. 9, pp. 1589-1592 (1993).
3. Everard, J. K. A. and Cheng, K. K. M., "High performance direct coupled bandpass filters on coplanar waveguide," *IEEE Transactions on Microwave Theory and Techniques*, Vol. 41, No. 9, pp. 1568-1573 (1993).
4. Gao, J. and Zhu, L., "Accurate circuit models of CPW coupling elements for the design of compact quarter-wavelength band-pass filters," *International Journal of RF and Microwave Computer-Aided Engineering*, Vol. 14, No. 5, pp. 453-461 (2004).
5. Ghione, G. and Naldi, C. U., "Coplanar waveguides for MMIC applications: effect of upper shielding, conductor backing, finite-extent ground planes, and line-to-line coupling," *IEEE Transactions on Microwave Theory and Techniques*, Vol. 35, No. 3, pp. 260-267 (1987).
6. Gorur, A., "A novel coplanar slow-wave structure," *IEEE Microwave and Guided Wave Letters*, Vol. 4, No. 3, pp. 86-88 (1994).
7. Her, M. L., Wang, Y. Z. C., Chang, M., and Lin, K. Y., "Coplanar waveguide (CPW) defected ground structure (DGS) for bandpass filter application," *Microwave and Optical Technology Letters*, Vol. 42, No. 4, pp. 331-334 (2004).
8. Kong, Y. W. and Chew, S. T., "A miniaturized end-coupled filter using stepped-impedance resonators," *Microwave and Optical Technology Letters*, Vol. 42, No. 2, pp. 97-99 (2005).
9. Matthaei, G. L., Young, L., and Jones, E. M. T., *Microwave Filters, Impedance-Matching Networks, and Coupling Structures*, Artech House, 1980.
10. Sanada, A., Takehara, H., Yamamoto, T., and Awai, I., "λ/4 stepped-impedance resonator bandpass filters fabricated on coplanar waveguide," *Proceedings of IEEE MTT-S International Microwave Symposium*, pp. 385-388 (2002)
11. Zhang, H. and Chen, K. J., "A tri-section stepped-impedance resonator for cross-coupled bandpass filters," *IEEE Microwave and Wireless Components Letters*, Vol. 15, No. 6, pp. 401-403 (2005).
12. Zhu, L. and Wu, K., "Accurate circuit model of interdigital capacitor and its application to design of new quasi-lumped miniaturized filters with suppression of harmonic resonance," *IEEE Transactions on Microwave Theory and Techniques*, Vol. 48, No. 3, pp. 347-356 (2000).